Int J Adv Manuf Technol (2013) 69:1833–1840
DOI 10.1007/s00170-013-5158-8

ORIGINAL ARTICLE

The effect of austenitic interlayer on microstructure and mechanical behaviors in keyhole plasma transfer arc welding of ferritic stainless steel couple

Tanju Teker

Received: 25 February 2013 / Accepted: 25 June 2013 / Published online: 7 July 2013

Abstract In this study, AISI 430 ferritic stainless steel couple of 10 mm thickness was welded by keyhole plasma transferred arc welding (KPTAW) process with or without filler wire addition using AISI 316L austenitic stainless steel interlayer of 2 mm thickness. Welded joints were manufactured with constant traverse speeds (0.01 m/min) under two different welding currents (110 and 130 A) at two different plasma gas flow rates (1.1 and 1.2 l/min), nozzle diameter (2.4 mm), and a shielding gas flow rate (25 l/min). In order to determine the microstructural changes that occurred, the interface regions of the welded samples were examined by scanning electron microscopy (SEM), optic microscopy, X-ray diffraction, and energy dispersive spectrometry after KPTAW. Microhardness and V-notch impact tests were conducted to determine the mechanical properties of the welded samples. In addition, fracture surface was examined by SEM after impact test.

Keywords KPTAW · Interlayer · Microstructure · Mechanical properties

1 Introduction

The plasma transferred arc welding (PTAW) can be defined as a gas-shielded arc welding process where the coalescence of metals is achieved via the heat transferred by an arc which is created between a tungsten electrode and a workpiece. The arc is constricted by a copper alloy. The PTAW process can be used in two distinct operating modes, often described as the melt-in mode and the keyhole mode. The melt-in mode refers to a weld pool similar to that which typically forms in the gas tungsten arc welding (GTAW) process, where a bowl-shaped portion of the workpiece material that is under the arc is melted. Keyhole plasma transferred arc welding (KPTAW) offers significant advantages over conventional GTAW in terms of penetration depth, joint preparation, and thermal distortion [1]. Although its energy is less dense than laser beam welding and electron beam welding, KPTAW is more cost effective and more tolerant of joint preparation. The keyhole process is used to weld thicker materials such as 10-mm-thick stainless steel plates in one single pass. So, the KPTA is better in economic/properties than GMAW and GMAW-P [2]. KPTAW has found applications on the welding of structural steels, automobiles, airplanes, rockets, pressure vessels, large diameter pipes, space shuttles, and possibly on welding in space [3–6]. By forcing the plasma gas and arc through a constricted orifice, the torch delivers a high concentration of energy to a small area, giving higher welding speeds and producing welds with high penetration/width ratios, thus limiting the heat-affected zone (HAZ) dimensions [7]. As the welding parameters, plasma gas flow rate and welding current, welding speed, into the keyhole must be carefully balanced to maintain the keyhole and weld pool stability [5–8]. The process can be operated with or without a filler wire addition. The molten weld metal flows around the arc and resolidifies behind the keyhole as the torch traverse the workpiece [9].

AISI 430 steels comprise approximately one half of the SAE-AISI-type 400 series stainless steels. Along with other alloying elements, these steels contain from 12 to 30 wt% Cr. They are known for their excellent stress corrosion cracking resistance and good resistance to pitting. In general, the toughness and ductility of ferritic stainless steel welds are reported to be low due to carbide precipitations and large grain size of the fusion zone AISI 430. The welding heat leads to grain coarsening in the heat-affected zone and in the weld metal of ferritic stainless steels because they solidify directly from the liquid to the ferrite phase without any intermediate phase transformation. There have been attempts

T. Teker (✉)
Department of Materials Engineering, Faculty of Engineering, University of Adıyaman, 02040 Adıyaman, Turkey
e-mail: tteker@adiyaman.edu.tr

to grain refine the welds of these steels by the addition of elements such as Ti and Al [10]. The ability to join ferritic stainless steel both to itself and to other materials with conventional fusion welding processes such as gas tungsten, laser beam, and electron beam welding opens up the possibility of producing unexpected phase propagation and a series of negative metallurgical changes like sigma phase and grain coarsening occur in the HAZ. Therefore, extensive care and precautions, such as pre- and post-heat treatments or quick welding speeds, are required [11].

Austenitic stainless steels are extensively used for good resistance to corrosion. When these steels are to be welded to ferritic steels (e.g., dissimilar joints, clad steel joints), usually a stainless steel filler metal is provided and weld metal may be hot-crack sensitive.

To minimize this tendency, the composition of weld metal should preferably consist of an austenitic structure with small amount of ferrite. They are widely used not only for their corrosion resistance but also they are readily formable, fabricable, and durable [11, 12].

In the literature, limited research has been made on the PTAW of ferritic stainless steel. Ferritic stainless steel was joined by manual metal arc welding process using austenitic and duplex filler metals. GMAW process had been used for repair welding of cracked martensitic stainless steel using 316L austenitic filler wire and the results had been found to be satisfactory [13].

In the present study, AISI 430 ferritic stainless steel couple of 10 mm thickness were welded by the KPTAW process with or without filler wire addition using AISI 316L austenitic stainless steel interlayer of 2 mm thickness. The aim of this study was to investigate the effect of austenitic interlayer on penetration depth, microstructure, and mechanical behaviors.

2 Materials and method

In this study, AISI 430-type ferritic stainless steel plates of 10 mm thick were welded using KPTA welding technique both itself and using austenitic stainless steel interlayer of 2 mm thick. Samples were prepared in dimensions $100 \times 50 \times 10\ mm^3$ (AISI 430) and $100 \times 10 \times 2\ mm^3$ (AISI 316L). The chemical compositions of test materials are listed in Table 1. Welds were produced using plasma welding equipment in which the torch was fixed to an automatic mobile system to control both the travel speed and the nozzle/workpiece distance. Pure argon gas was used as both the shielding gas and the plasma gas. The operating principle of KPTAW system is schematically shown in Fig. 1a, b, and the process parameters for keyhole welding are given in Table 2. For metallographic examination, the welded samples were cut perpendicular to the bond interfaces using a low speed diamond saw. The cross sections of these joints were ground using a grit sequence of 200–1,200. These samples were mechanically polished using cloth and polishing solution of 3 μm diamond paste as a final polish and then cleaned using acetone. For microstructural examination, samples were etched electrolytically with a solution of 50 % HCl + 30 % H_2O + 20 % NHO_3. The

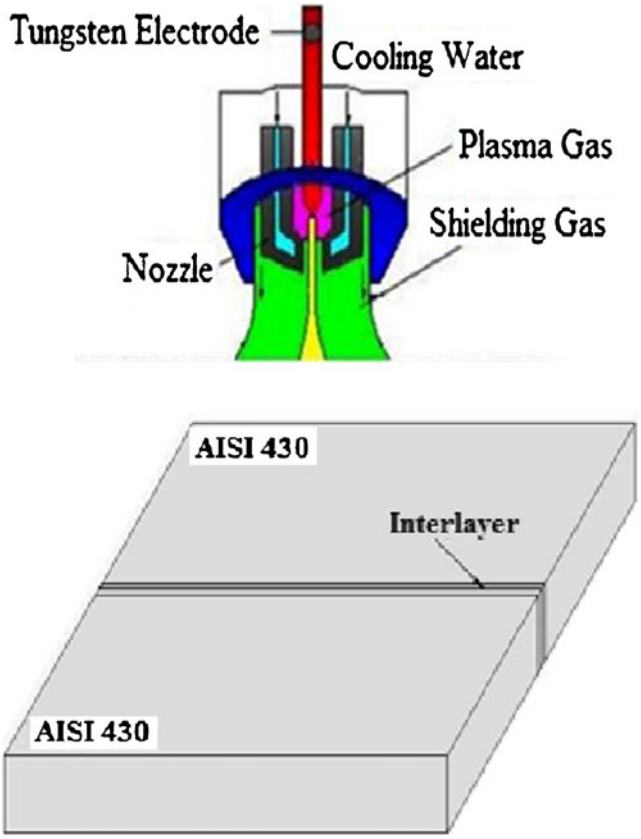

Fig. 1 The operating principle of keyhole plasma transferred arc welding process

Table 1 The chemical compositions of the materials

Chemical compositions (wt%)								
Alloy	Fe	Cr	C	Ni	Si	Mo	S	Mn
AISI 430	Bal.	16.02	0.048	0.22	0.44	0.016	0.002	0.610
AISI 316L	Bal.	18	0.03	12	0.7	2.5	–	0.8

Table 2 The process parameters used in keyhole plasma transferred arc welding

Sample no.	Welding current (A)	Plasma gas flow rate (l/min)	Shielding gas flow rate (l/min)	Welding speed (m/min)	Nozzle diameter (mm)	Austenitic interlayer
S1	110	1.1	25	0.01	2.4	Without
S2	110	2	25	0.01	2.4	With
S3	130	1.1	25	0.01	2.4	Without
S4	130	2	25	0.01	2.4	With

microstructure properties in the welding interface of the welded samples were investigated by optical microscopy (OM) and scanning electron microscope (SEM: JEOL JSM 7001 F) device. Energy dispersive spectrometry (EDS) analysis was also done to pick up the elemental content of the phases which were formed at the interface of the welded samples. In order to determine the phases and compounds on samples, X-ray diffraction analysis (XRD) analysis was performed using XRD-6000 equipped with a Cu $K\alpha$/tube, wave length of α=1.54056 Å, voltage of 40 kV, and ampere of 40 mA. Microhardness measurements of samples were carried out at an interval of 0.5 mm on load of 200 g with HV hardness scale. Leica MHT-10 testing machine was used for measurements. Impact test samples were prepared to dimensions of $55\times10\times10$ mm^3 and then the samples were tested using a Wolpert PW30 V-notch impact test device with a hammer of 300 J. The fractured surface of impact tested samples was analyzed using SEM at higher magnification to study the fracture morphology to establish the nature of the fracture.

3 Results and discussions

3.1 Macro and microstructure characteristics

Figure 2a–d shows the widths of welding surface of samples welded by KPTAW process using the two different welding currents, plasma gas flow rate, and the a constant—the nozzle orifice diameter of 2.4 mm. As can be seen in the figure, the widths of weld metal surface in the samples S1, S2, S3, and S4 are approximately S1=5, S2=6, S3=9, and S4=10 mm. Figure 3a–d shows the penetration depth of the samples S1, S2, S3, and S4 (with and without austenitic interlayer material) which is joined by KPTAW process, respectively. As it can be seen in the Fig. 3, the penetration depths in the welded samples were obtained as S1=4, S2=5, S3=6, and S4=7 mm. These results show that welding current and plasma gas flow rate are an important parameter in the KPTAW [14, 15]. One hundred thirty-ampere current input and plasma gas flow of 2 l/min are more intensive than plasma gas flow rate of

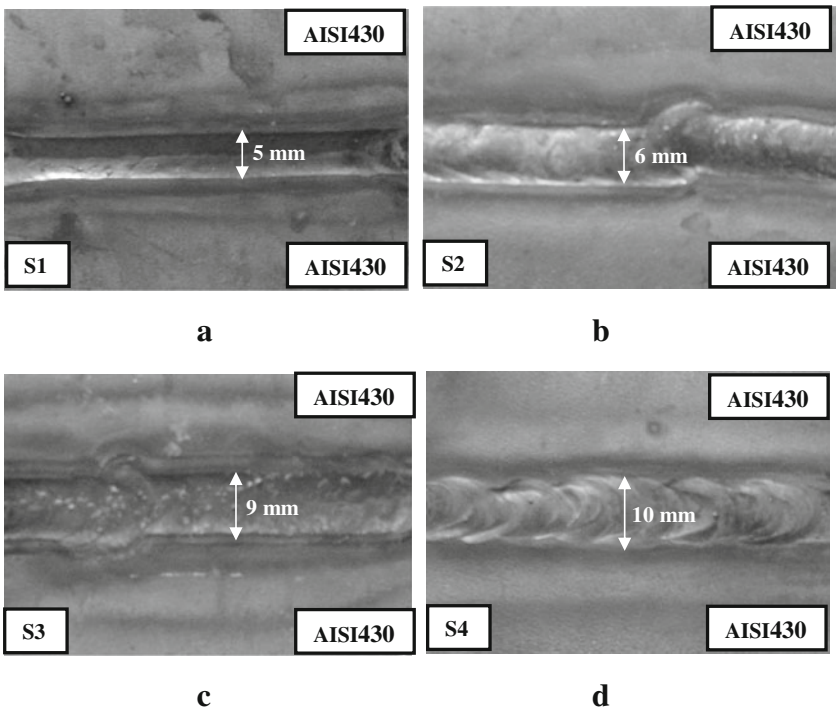

Fig. 2 The surface macro photographs of welded samples

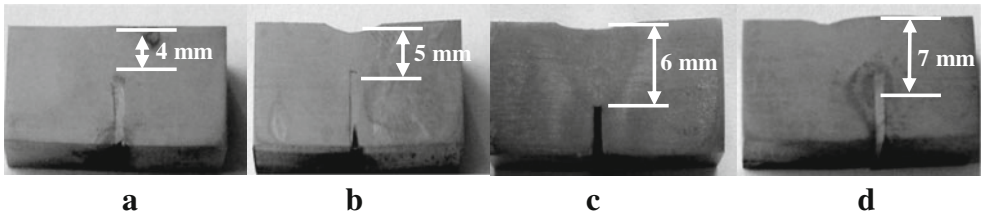

Fig. 3 The cross-sectional macro photographs of welded samples

1.1 l/min, and therefore, the welding penetration depth is higher. By the increase of the welding current and plasma gas flow rate, the obtained higher heat input results to an increase in the width and penetration depth of weld metal.

Figure 4a, b show SEM and OM micrographs of microstructural changes occurred at the interface of welded sample S3. In the KPTAW of the sample S3, austenitic interlayer was not used. As shown in the figures, the weld metal consisted of plate martensite. Because of inadequate diffusion time, the austenite may transform to martensite during cooling. The micrographs of weld metal (Fig. 4) exhibit microstructure of coarse ferrite grains with randomly distributed carbides as seen from result of XRD analyses. A two-phase ferrite plus matensite fusion zone microstructure is shown in Fig. 4. The martensite is present along the ferrite grain boundaries and is generally present as a continuous grain boundary phase. Ferritic stainless steel-welded samples exhibit a fine dispersion of precipitates within the ferrite or at the ferrite–martensite boundary. A similar precipitation behavior is observed in the HAZ. Very fine equiaxed ferrite grains with grain boundary (lath type) martensite are observed in HAZ. On the HAZ side, the zone containing coarse grains which comprised ferrite phases and chromium carbides also included intense amount of chromium carbide in specifically intragranular (pepper-like) forms as shown in Fig. 4. Since weld microstructure is greatly influenced by chemical composition, the chromium equivalent and nickel equivalent based on Schaffler diagram [16] for ferritic–martensitic stainless steel are calculated using the Eqs. (1) and (2). Ferrite and martensite are expected in the weld metal by examination of Cr_{Eq} and Ni_{Eq} values on the constitution diagram.

$$Cr_{Eq} = \%Cr + \%Mo + 1.5\%Si + 0.5\%Nb \quad (1)$$

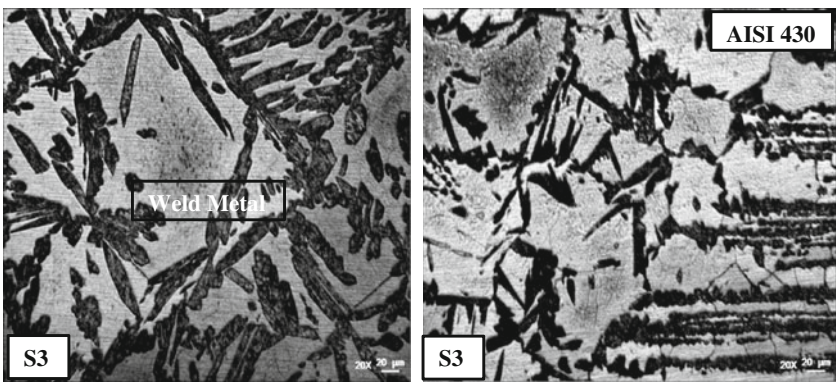

a

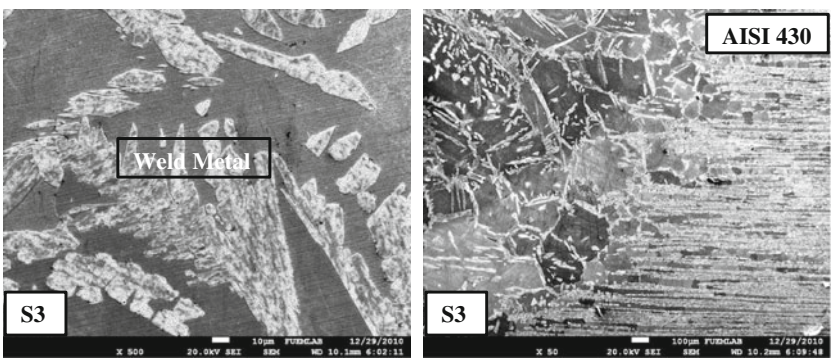

b

Fig. 4 **a** Optical micrograph of the weld metal and transition zone of sample S3. **b** The SEM micrographs taken from the welding interface of sample S3

$$Ni_{Eq} = \%Ni + 30\%C + 0.5\%Mn \quad (2)$$

$$Cr_{Eq} = 16.69 = \tilde{}17 \qquad Ni_{Eq} = 1.96 = \tilde{}2$$

Figure 5a, b shows the SEM and OM micrographs of microstructural changes that occurred at the interface of welded sample S4. From the micrograph, it is clearly seen that the microstructure of fusion zone consists of austenite and martensite phases. Generally, a variety of structures are formed during solidification of weld metal, depending on compositions of filler and base metals [12]. SEM micrographs and EDS analysis of the welded joint S4 are presented in Fig. 6a, b. As it can be seen in the Fig. 6, a different phase is seen in the fusion zone. This phase consists of 80.69 wt% Fe, 2.68 wt% C, 15.04 wt% Cr, 1.06 wt% Ni, and 0.53 wt% Si according to the EDS analysis (Fig. 6b). This composition was detected as γ-austenite from the Fe-Cr-Ni ternary phase diagram. Additionally, from the microstructure in Fig. 5, lath martensite is seen within the matrix. The results of XRD analysis for the welded joints S3 and S4 are shown in Fig. 7a, b. From the results of XRD analysis, ferrite (α), Fe_3C, Fe_7C_3, Cr_7C_3, and Cr_3C_2 carbides compounds were seen on the weld metal of welded joints.

The microhardness measurements taken from the cross section of the weld metal are seen in Fig. 8 for sample 3 (without interlayer) and sample 4 (with interlayer). As seen in Fig. 8, significantly similar patterns were observed in the microhardness profiles of the samples. Formation of chrome carbide phases and a martensitic structure in the intermediate zone as a result of rapid cooling increased the hardness across the weld seam zone. Due to this result, higher microhardness values were observed across the weld seam. The hardness of the welding zone was varying from 408 to 492 HV, which is higher than the base material (160–200 HV). With KPTA method ensuring higher energy input, a more uniform distribution of intensive carbide formation and presence of other hard phases in the microstructure positively affected the hardness. Furthermore, higher microhardness values obtained across the weld result from the incomplete dendritic structure formation in small proportions due to rapid cooling. The hardness values in fusion zone are higher than HAZ with and without austenitic interlayer samples. The highest hardness in the HAZ occurs in the region where carbide distribution is almost equal. From Fig. 8, it is clearly seen that fusion zone hardness values in the sample with interlayer are lower than the sample without austenitic interlayer. Carbide formation decreases as the carbon content of fusion zone decrease by austenitic interlayer. This result shows that the austenitic interlayer in the KPTAW causes low hardness in fusion zone.

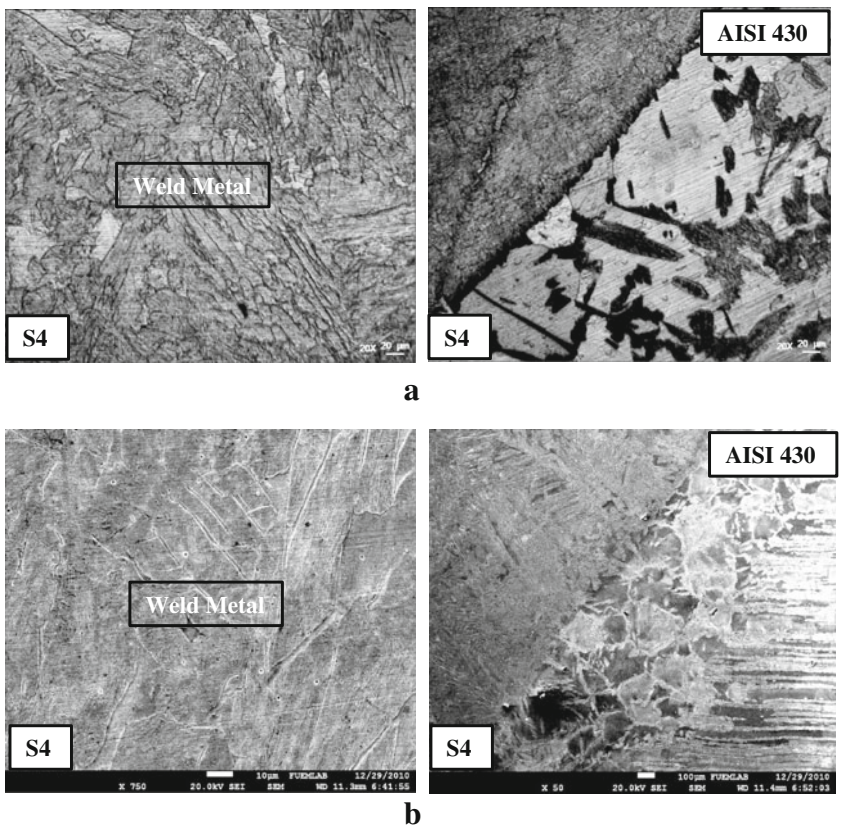

Fig. 5 **a** Optical micrograph of the weld metal and transition zone of sample S4. **b** The SEM micrographs taken from the welding interface of sample S4

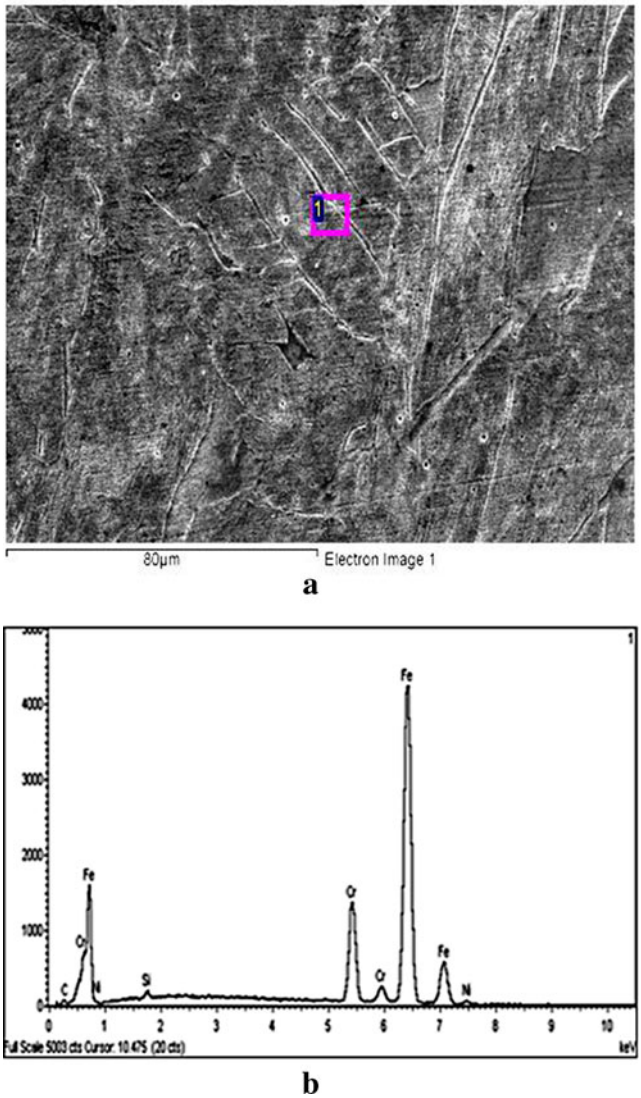

Fig. 6 SEM micrographs and EDS analysis of sample S4

3.2 Mechanical characterization

The impact toughness of the welded joints were obtained as S1=5 J, S2=8 J, S3=9 J, and S4=15 J. These results show that austenitic interlayer in the KPTAW of ferritic stainless steel increases the impact strength. Also, depending on increasing energy input and plasma gas flow rate, an increase was noticed in the notch impact values of the welded joints. This may be attributed to the fact that the penetration depth increased due to higher temperatures and energy density resulting from increasing plasma gas flow rate and a rise in temperature. Existence and size of the unwelded section on the interface of the two metal pair creates a notch effect and, therefore, play a significant role on the results of the notch impact tests carried out [15]. Austenitic stainless steel weld metal predominates compared to ferritic stainless steels in terms of toughness and ductility. During welding of ferritic stainless steel, the formation and nature of chromium carbide

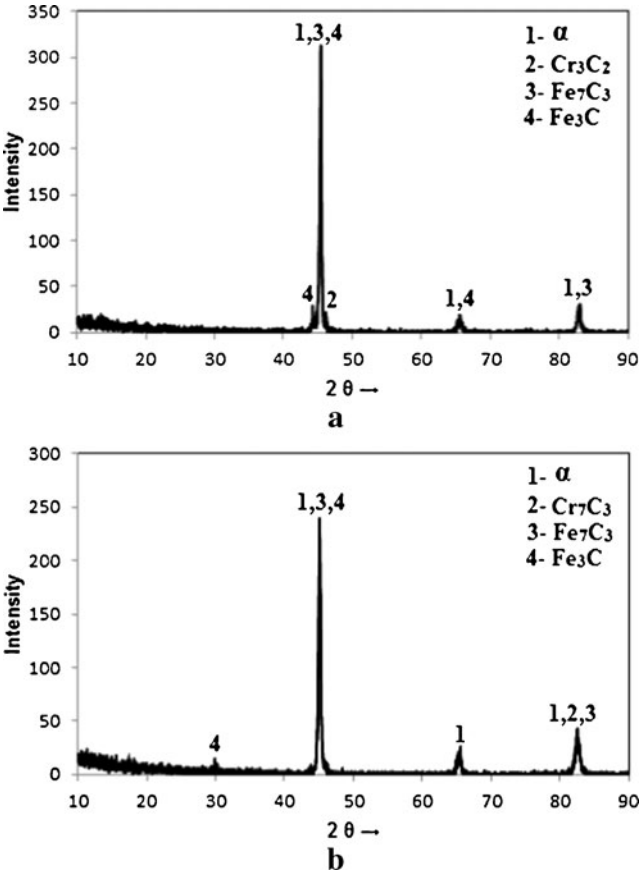

Fig. 7 X-ray diffraction analyses for **a** S3 and **b** S4 samples

in HAZ unfavorably affects the toughness and ductility of the weld joints, particularly when coupled with coarse grain size. Carbide formation and distribution decreased and martensite formation morphology changed in welded sample with interlayer. As a result, the sample with interlayer has higher impact strength than without interlayer. Austenitic stainless steel is predominating compared to ferritic stainless steels in terms of toughness and ductility. Besides, brittleness

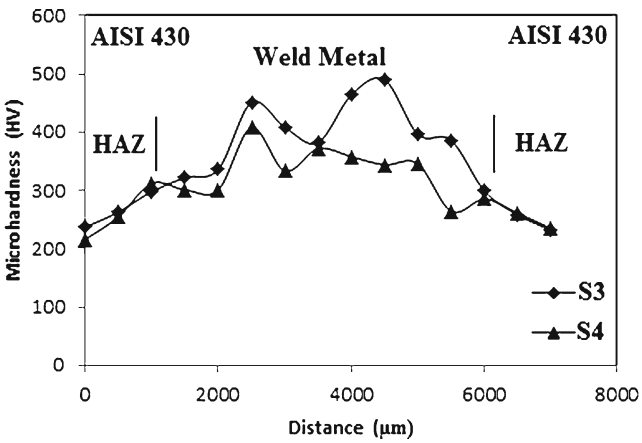

Fig. 8 Microhardness distribution from the HAZ to weld metal in samples 3 and 4

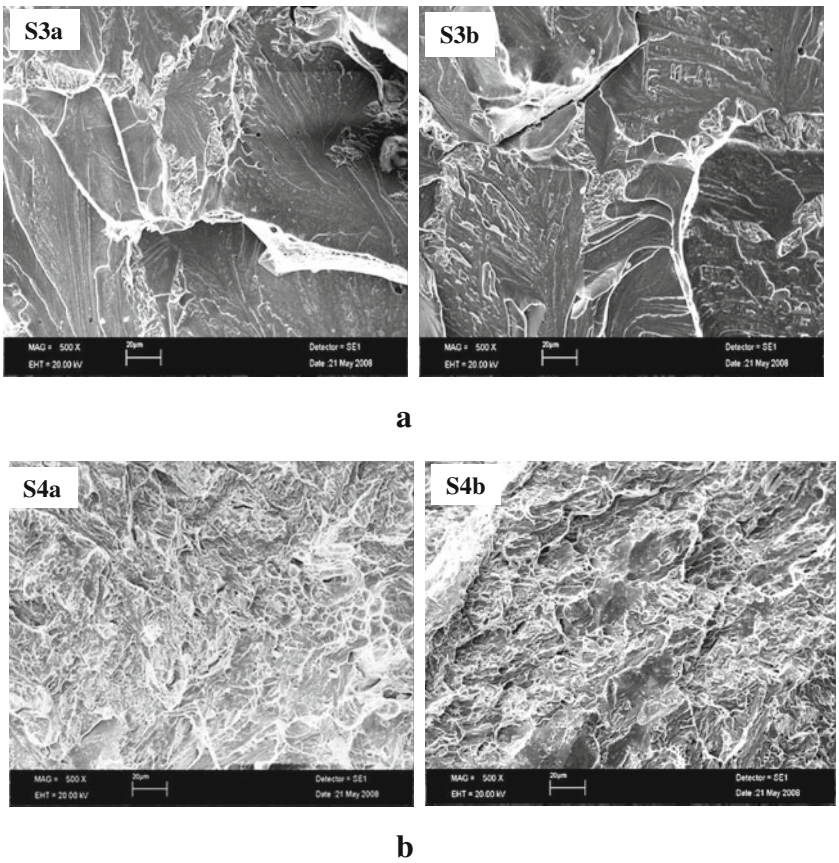

Fig. 9 SEM micrographs of fracture surfaces after notch impact test of welded samples. **a** S3 and **b** S4 samples

caused by grain growth is prevented using austenitic interlayer. Austenitic stainless steels are also used and will result in a two-phase, austenit + ferrite microstructure that has superior ductility and toughness relative to a ferritic stainless steel deposit.

3.3 Fractography

The fractured surface morphology of impact test samples were analyzed using SEM. Figure 9a shows the images of fracture surfaces resulting from the impact test of the welded joints of sample S3. As it can be seen in the figure, fracture occurred in AISI 430 side widely and it is observed that the broken grains have a crystalline fish back appearance. The samples display a brittle fracture mechanism. For ferritic stainless steels, the fracture morphology is an intergranular crack which is peculiar to brittle fracture and it is reported that HAZ and the welding metal have excessive grain coarsenings. Figure 9b shows the images of fracture surfaces resulting from the impact test of the welded joints of S4 sample. As it can be seen in the figure, the fracture surface of sample S4 shows ductile fracture and elongated fine dimples. These fine dimples are a characteristic feature of ductile fracture. That is due to austenitic stainless steel interlayer because austenitic stainless steel is more ductile than ferritic stainless steel.

4 Conclusions

AISI 430 ferritic stainless steel couple of 10 mm thickness was joined by KPTAW process with or without filler wire addition using austenitic stainless steel interlayer of 2 mm thickness. The following important conclusions are derived from this examination:

1. The maximum penetration depth of 7 mm was obtained using interlayer. The weld width and penetration depth of the weld metal were mainly affected by high energy input and plasma gas flow rate. Austenitic interlayer caused austenite phase and lath martensite in the fusion zone. Carbide formation and distribution decreased and martensite formation morphology changed in welded samples with interlayer.
2. The hardness values in the samples with interlayer are lower than the hardness values of the samples without austenitic interlayer. The samples with austenitic interlayer have higher impact strength. The fracture surface of welded samples with interlayer showed ductile

fracture. The samples without interlayer displayed a brittle fracture mechanism.

References

1. Tomsic M, Barhorst S (1984) Keyhole plasma arc welding of aluminum with variable polarity power. Weld J 63(2):25–32
2. Hsu YF, Rubinsky B (1988) Two-dimensional heat transfer study on the keyhole plasma arc welding process. Int J of Heat Mass Trans 31(7):1409–1421
3. Martikainen J (1995) Conditions for achieving high-quality welds in the plasma-arc keyhole welding of structural steels. J Mater Process Technol 52(1):68–75
4. Vilkas EP (1991) Plasma arc welding of exhaust pipe system components. Weld J 70(4):49–52
5. Irving B (1992) Plasma arc welding takes on the advanced solid rocket motor. Weld J 71(12):49–50
6. Keanini RG, Rubinsky B (1990) Plasma arc welding under zero and normal gravity. Weld J 69(6):41–50
7. Craig E (1988) The plasma arc welding a review. Weld J 67(2):19–25
8. Tomsic MJ, Jackson CE (1974) Energy distribution in keyhole mode plasma arc welds. Weld J 53(3):109–115
9. Harris ID (1993) Welding brazing and soldering. ASM Metals Handbook, Materials Park, OH., 6: pp 195
10. Brooks JA, Thompson AW, Williams JC (1984) A fundamental study of the beneficial effects of delta ferrite in reducing weld cracking. Weld J 63(3):71–83
11. Lippold JC, Kotecki DJ (2005) Welding metallurgy and weldability of stainless steels. Wiley, Hoboken, pp 88–135
12. Lakshminarayanan AK, Shanmugam K, Balasubramanian V (2009) Effect of autogenous arc welding processes on tensile and impact properties of ferritic stainless steel joints. J Iron Steel Res Int 16(1):62–68
13. Bhaduri AK, Gill TPS, Albert SK, Shanmugam K, Iyer DR (2001) Repair welding of cracked steam turbine blades using austenitic and martensitic stainless-steel consumables. Nuclear Eng Des 249–259
14. Teker T, Ozdemir N (2012) The effect of current intensity on penetration deep of AISI 430/AISI 1040 steel couple welded by keyhole plasma transfer arc welding process. Int Iron & Steel Symp IISS'12, Karabük, Turkey, April, University of Karabük, pp. 762–768
15. Teker T, Ozdemir N (2012) Weldability and joining characteristic of AISI 430/AISI 1040 steel using keyhole plasma arc welding. Int J Adv Manuf Technol 63(1–4):117–128
16. Balmforth MC, Lippold JC (2000) A new ferritic–martensitic stainless steel constitution diagram. Weld J 77(1):1–7